

Comparison of the generalized Riemann solver and the gas-kinetic scheme for inviscid compressible flow simulations

Jiequan Li^a, Qibing Li^b, Kun Xu^{c,*}

^a School of Mathematical Sciences, Beijing Normal University, 100875, China

^b Department of Engineering Mechanics, Tsinghua University, 100084, China

^c Department of Mathematics, Hong Kong University of Science and Technology, Kowloon, Hong Kong

ARTICLE INFO

Article history:

Received 3 November 2010

Received in revised form 10 February 2011

Accepted 15 March 2011

Available online 8 April 2011

Keywords:

Generalized Riemann problem

Gas kinetic scheme

Inviscid Euler equations

Non-equilibrium flows

ABSTRACT

The generalized Riemann problem (GRP) scheme for the Euler equations and gas-kinetic scheme (GKS) for the Boltzmann equation are two high resolution shock capturing schemes for fluid simulations. The difference is that one is based on the characteristics of the inviscid Euler equations and their wave interactions, and the other is based on the particle transport and collisions. The similarity between them is that both methods can use identical MUSCL-type initial reconstructions around a cell interface, and the spatial slopes on both sides of a cell interface involve in the gas evolution process and the construction of a time-dependent flux function. Although both methods have been applied successfully to the inviscid compressible flow computations, their performances have never been compared. Since both methods use the same initial reconstruction, any difference is solely coming from different underlying mechanism in their flux evaluation. Therefore, such a comparison is important to help us to understand the correspondence between physical modeling and numerical performances. Since GRP is so faithfully solving the inviscid Euler equations, the comparison can be also used to show the validity of solving the Euler equations itself. The numerical comparison shows that the GRP exhibits a slightly better computational efficiency, and has comparable accuracy with GKS for the Euler solutions in 1D case, but the GKS is more robust than GRP. For the 2D high Mach number flow simulations, the GKS is absent from the shock instability and converges to the steady state solutions faster than the GRP. The GRP has carbuncle phenomena, like a cloud hanging over exact Riemann solvers. The GRP and GKS use different physical processes to describe the flow motion starting from a discontinuity. One is based on the assumption of equilibrium state with infinite number of particle collisions, and the other starts from the non-equilibrium free transport process to evolve into an equilibrium one through particle collisions. The different mechanism in the flux evaluation deviates their numerical performance. Through this study, we may conclude scientifically that it may NOT be valid to use the Euler equations as governing equations to construct numerical fluxes in a discretized space with limited cell resolution. To adapt the Navier–Stokes (NS) equations is NOT valid either because the NS equations describe the flow behavior on the hydrodynamic scale and have no any corresponding physics starting from a discontinuity. This fact alludes to the consistency of the Euler and Navier–Stokes equations with the continuum assumption and the necessity of a direct modeling of the physical process in the discretized space in the construction of numerical scheme when modeling very high Mach number flows. The development of numerical algorithm is similar to the

* Corresponding author. Tel.: +852 2358 7440; fax: +852 2358 1643.

E-mail addresses: jiequan@bnu.edu.cn (J. Li), lqb@tsinghua.edu.cn (Q. Li), makxu@ust.hk (K. Xu).

modeling process in deriving the governing equations, but the control volume here cannot be shrunk to zero.

© 2011 Elsevier Inc. All rights reserved.

1. Introduction

The modern computational fluid dynamics (CFD) method for compressible flow is based on the Riemann problem from piecewise constant states [14]. The necessity to use discontinuous initial condition is due to the limited cell resolution to represent physical flow structure. Due to the preparation of discontinuous initial data through the so-called nonlinear limiter, the numerical dissipation is implicitly added in the shock capturing schemes. In the past decades, the shock capturing CFD methods based on the exact or approximate Riemann problems are extremely successful in the engineering applications and the scientific study of compressible flows. In order to further increase the accuracy, generalized Riemann solvers under piecewise linear discontinuous initial data were developed. The generalized Riemann problem (GRP) was proposed for compressible flows based on the Lagrangian formulation first [2,4], and a direct Eulerian version was developed in [6,5] using the concept of Riemann invariants. Theoretically, in the GRP, a close coupling between the spatial and temporal evolution is recovered through the analysis of detailed wave interactions. The GRP is more precise and accurate than any other approximate Riemann solvers. It is the most accurate description of the Euler solutions under its corresponding initial condition. The schemes based on the GRP have been applied successfully to many engineering problems [1,3,12,13,18].

On the other hand, based on the gas-kinetic theory, the Euler and Navier–Stokes equations can be derived from the Boltzmann equation using the Chapman–Enskog expansion [9]. In a gas-kinetic representation, all flow variables are moments of a single particle distribution function. In the past years, a gas-kinetic scheme (GKS) based on the BGK model [7] has been developed for the compressible flow simulation under linear polynomials for the mass, momentum, and energy distributions separated by discontinuities at the origin [32,23]. The GKS has been successfully applied in many engineering applications, especially for the hypersonic viscous and heat conducting flows [33,20,21].

In this paper, we are going to compare the performance of GRP and GKS in many 1D and 2D flow computations, especially to the test cases on which many other schemes may have difficulties, e.g. the large density ratio problem [27], highly expansion wave, and the blunt body problem. Since GRP and GKS use the identical initial reconstruction and follow explicitly their time evolution within a time step, any difference between these two methods must come from the dynamic mechanism in their flux construction. The GRP and GKS are following different physical processes in the description of flow motion starting from a discontinuity. Their comparison definitely gives us useful information about the correspondence between the physical modeling and numerical performance. This is also the main reason why we do not use other Riemann solvers. For many other Riemann solvers, the problem is that either the real governing equations are unknown, or they are constructed in an ad hoc ways. The GRP truthfully follows the Euler solution and it has the most accurate Euler flux under the corresponding initial condition.

Based on the comparison and analysis in this paper, we come into the following conclusion. For algorithm development, the direct physical modeling of the gas evolution process in a discretized space is more fundamental and important than adapting any presumed governing equation from the start point. The Euler equations can be only used to describe the equilibrium flow, which is incapable to describe the non-equilibrium effects inside a numerical strong shock layer. Due to the cell resolution, the non-equilibrium flow region has been numerically enlarged. The physical process in the GRP is inadequate in describing the flow behavior in this region. As a result, the carbuncle phenomenon is intrinsically rooted in the exact Riemann solver. Since GRP is so accurate in solving the Euler equations, through this research we would like to raise the questions about the validity of directly using a governing equation which has infinite wave resolution to a space with limited cell size and time step. Due to the inclusion of both kinetic and hydrodynamic scale physics in the kinetic formulation, the GKS provides a more reliable gas evolution model than GRP to describe flow starting from a discontinuity. We hope that through this study and any other following up research, the CFD will evolve from an art-based to a science-based research subject.

2. Generalized Riemann problem and gas-kinetic schemes

In this paper we will focus on the comparison of numerical results for the compressible Euler equations,

$$\begin{aligned} \mathbf{u}_t + \mathbf{F}(\mathbf{u})_x + \mathbf{G}(\mathbf{u})_y &= 0, \\ \mathbf{u} &= (\rho, \rho U, \rho V, \rho E)^\top, \\ \mathbf{F}(\mathbf{u}) &= (\rho U, \rho U^2 + p, \rho UV, U(\rho E + p))^\top, \\ \mathbf{G}(\mathbf{u}) &= (\rho V, \rho UV, \rho V^2 + p, V(\rho E + p))^\top, \end{aligned} \quad (1)$$

where ρ , $(\rho U, \rho V)$ and ρE are conserved variables of the density, the momentum and the total energy with $E = \frac{U^2 + V^2}{2} + e$, e the internal energy, p is the pressure and $p = (\gamma - 1)\rho e$ for polytropic gases. Then following the finite volume formulation, we write (1) as

$$\mathbf{u}_j^{n+1} = \mathbf{u}_j^n - \frac{1}{|\Omega_j|} \sum_{i=1}^m \int_{t^n}^{t^{n+1}} F_{ij} dt, \quad (2)$$

where Ω_i is the control volume with sides $\Gamma_{ij}, j = 1, \dots, m$ ($m = 4$ in this paper), $\mathbf{n} = (n_{j1}, n_{j2})$ is the outer normal of Γ_{ij} , and the numerical flux F_{ij} is

$$F_{ij} = \int_{\Gamma_{ij}} (\mathbf{F}, \mathbf{G})(\mathbf{u}) \cdot (n_{i1}, n_{i2}) d\Gamma, \quad (3)$$

where \mathbf{u}_j^n is the usual average of $\mathbf{u}(x, t_n)$ over Ω_j . In one-dimensional case, $\Omega_j = (x_{j-\frac{1}{2}}, x_{j+\frac{1}{2}})$ and the center $x_j = (x_{j-\frac{1}{2}} + x_{j+\frac{1}{2}})/2$. The GRP and GKS both provide a respective time-dependent flux function from a piecewise linear discontinuous initial data. In this section, we are going to first present the reconstruction used in the present paper.

As expressed in (2), at the beginning of each time step $t = t_n$ only cell averaged mass, momentum and energy densities are given. As far as a high-resolution scheme is concerned, interpolation techniques are used to construct the subcell structure. Simple polynomials usually generate spurious oscillations if large gradients exist in the data. The most successful interpolation techniques known so far are those based on the concepts of limiters [8,29], and these interpolation rules can be applied to the conservative, characteristic or primitive flow variables. In this paper, the reconstruction is solely applied to the conservative variables. The limiter used is the van Leer limiter. With the cell averaged component of conservative variables w_j , and their differences between neighboring cells $s_+ = (w_{j+1} - w_j)/\Delta x$ and $s_- = (w_j - w_{j-1})/\Delta x$, the slope of w in cell j is constructed as

$$L(s_+, s_-) = S(s_+, s_-) \frac{|s_+||s_-|}{|s_+| + |s_-|},$$

where $S(s_+, s_-) = \text{sign}(s_+) + \text{sign}(s_-)$. After reconstruction, the flow variable w is distributed linearly in cell j ,

$$\bar{w}_j(x) = w_j + L(s_+, s_-)(x - x_j), \quad x_{j-\frac{1}{2}} < x < x_{j+\frac{1}{2}}.$$

The interpolated flow distribution around a cell interface is shown in Fig. 1. Both the GRP and GKS are based on the above initial data to evaluate a time-dependent local solution.

2.1. The Generalized Riemann problem for the inviscid Euler equations

The generalized Riemann problem (GRP) scheme starts directly from (1). Denote by P_{ij} the middle point of Γ_{ij} and $F_{ij} = (\mathbf{F}, \mathbf{G}) \cdot (n_{i1}, n_{i2})$. Then the GRP uses the middle point value to directly approximate the flux $F_{ij}^{n+\frac{1}{2}}$, within the accuracy of second order,

$$F_{ij}^{n+\frac{1}{2}} \sim F_{ij} \left(\mathbf{u} \left(P_{ij}, \left(n + \frac{1}{2} \right) \Delta t \right) \right). \quad (4)$$

One of main issues is how to calculate the mid-point value $\mathbf{u}(P_{ij}, (n + \frac{1}{2})\Delta t)$ using as much characteristics of (1) as possible. Here we use the Taylor series expansion,

$$\mathbf{u}(P_{ij}, (n + \frac{1}{2})\Delta t) = \mathbf{u}(P_{ij}, t_n + 0) + \frac{\Delta t}{2} \frac{\partial \mathbf{u}}{\partial t}(P_{ij}, t_n + 0) + \mathcal{O}(\Delta t^2). \quad (5)$$

Fix the cell interface Γ_{ij} and denote by

$$\mathbf{u}_* = \mathbf{u}(P_{ij}, t_n + 0), \quad \left(\frac{\partial \mathbf{u}}{\partial t} \right)_* = \frac{\partial \mathbf{u}}{\partial t}(P_{ij}, t_n + 0). \quad (6)$$

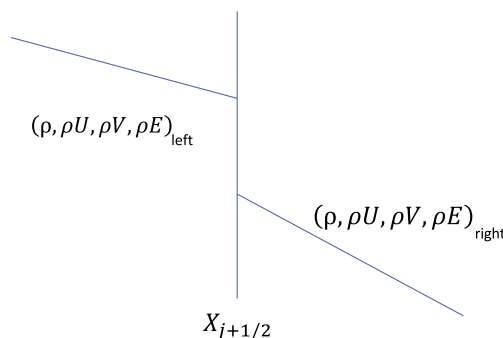


Fig. 1. The reconstructed initial conservative variables around a cell interface.

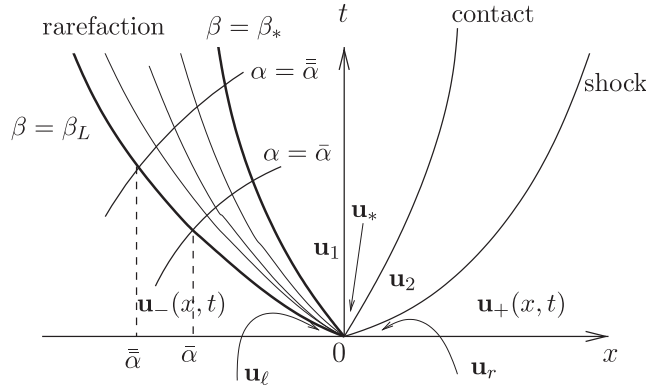


Fig. 2. A typical wave pattern for the GRP. The initial data $\mathbf{u}_0(x) = \mathbf{u}_\ell + x\mathbf{u}'_\ell$ for $x < 0$ and $\mathbf{u}_0(x) = \mathbf{u}_r + x\mathbf{u}'_r$ for $x > 0$.

The first instantaneous value \mathbf{u}_* is obtained with the standard Riemann solver [4,28]. The main contribution of the GRP scheme is how to obtain the instantaneous value of time derivative $(\partial\mathbf{u}/\partial t)_*$ analytically, which boils down to solving the associated generalized Riemann problem along each cell interface Γ_{ij} . For this purpose, we shift (P_{ij}, t_n) to the coordinate origin $(0, 0, 0)$ and make Γ_{ij} coincide with the y -axis. Then we define the quasi-one-dimensional (planar) generalized Riemann problem for

$$\mathbf{u}_t + \mathbf{F}(\mathbf{u})_x = 0, \quad (7)$$

subject to the initial data

$$\mathbf{u}(x, y, 0) = \begin{cases} \mathbf{u}_\ell + x\mathbf{u}'_{\ell\ell} + y\mathbf{u}'_{\ell y}, & x < 0, \\ \mathbf{u}_r + x\mathbf{u}'_{r\ell} + y\mathbf{u}'_{ry}, & x > 0, \end{cases} \quad (8)$$

where $\mathbf{u}_\ell, \mathbf{u}'_{\ell\ell}, \mathbf{u}'_{\ell y}, \mathbf{u}_r, \mathbf{u}'_{r\ell}, \mathbf{u}'_{ry}$ are constant vectors. In particular, as $\mathbf{u}'_{\ell y}$ and \mathbf{u}'_{ry} vanishes, Eq. (8) becomes planar one-dimensional flows. The conventional GRP solver uses the planar one-dimensional Euler equations (7) for simplicity and efficiency. Then we assume the wave configuration from the y -axis as shown in Fig. 2, in which a curved rarefaction wave moves to the left, a shock to the right and the t -axis is located in the intermediate region. Other cases can be treated similarly. We remind that as the initial data is uniform, i.e., piecewise constant, the rarefaction wave in Fig. 2 becomes isentropic, referred as a centered rarefaction wave (CRW). As the initial data is not uniform the instantaneous value of time derivative $(\partial\mathbf{u}/\partial t)_*$ can be solved in the following proposition.

Proposition 1. Let $(\partial\mathbf{u}/\partial t)_*$ be the instantaneous time derivative of \mathbf{u} evaluated at the origin. Then $(\partial U/\partial t)_*$ and $(\partial p/\partial t)_*$ are determined by solving a pair of linear equations

$$\begin{aligned} a_\ell \left(\frac{\partial U}{\partial t} \right)_* + b_\ell \left(\frac{\partial p}{\partial t} \right)_* &= d_\ell, \\ a_r \left(\frac{\partial U}{\partial t} \right)_* + b_r \left(\frac{\partial p}{\partial t} \right)_* &= d_r, \end{aligned} \quad (9)$$

where the coefficients a_ℓ, b_ℓ and d_ℓ depends on $\mathbf{u}_*, \mathbf{u}_\ell$ and \mathbf{u}'_ℓ ; and a_r, b_r and d_r depends on $\mathbf{u}_*, \mathbf{u}_r$ and \mathbf{u}'_r . The instantaneous time derivative of the density ρ is given by the state equation $p = p(\rho, S)$, S is the entropy,

$$dp = c^2 d\rho + \frac{\partial p}{\partial S} dS. \quad (10)$$

The velocity component V satisfies

$$V_t + UV_x = 0. \quad (11)$$

It resembles the entropy variable S (cf. (17) below) and can be treated similarly.

All these coefficients can be obtained explicitly as presented in [6]. It turns out that the coding process is almost the same as a 2×2 linear system that we will show below. In the derivation of this proposition, the fundamental idea is to extract singularities (discontinuities) from the complex wave patterns:

$$\text{Wave patterns} = \text{a singular part} + \text{a regular part}. \quad (12)$$

The GRP scheme expresses and manipulates the regular part using Riemann invariants and leave the singular part aside. This manipulation is indispensable. Below is a heuristic example of a linear toy system in order to explain (12) clearly,

$$\begin{aligned} u_t + av_x &= 0, \\ v_t + au_x &= 0, \end{aligned} \quad (13)$$

where $a > 0$ is a constant. In consistent with the notations in (8), $\mathbf{u} = (u, v)^\top$ here. In order to develop the second order MUSCL-type (upwind) scheme for (13), the piecewise linear data is given

$$\mathbf{u}(x, 0) = \begin{cases} \mathbf{u}_\ell + x\mathbf{u}'_\ell, & x < 0, \\ \mathbf{u}_r + x\mathbf{u}'_r, & x > 0 \end{cases} \quad (14)$$

and we need to know the intermediate value $\mathbf{u}(0, t)$ along the t -axis. Note that the initial data contains a discontinuity at the origin, causing nontrivial singularities (discontinuities) that propagate along characteristics $x = \pm at$, which implies that both the variables u and v are discontinuous across $x = \pm at$. In order to cope with this difficulty, it is necessary to extract out the singularities in some sense. For this purpose, we make the following manipulation for (13)

$$\begin{aligned} (u + v)_t + a(u + v)_x &= 0, \\ (u - v)_t - a(u - v)_x &= 0. \end{aligned} \quad (15)$$

Then the assembled quantity $u + v$ is continuous in the region $\{(x, t); x < at, t > 0\}$ although both u and v are discontinuous across $x = -at$. The same is true for $u - v$ in the region $\{(x, t); x > -at, t > 0\}$. Thus we use $u + v$ and $u - v$ as new dependent variables to easily obtain

$$\begin{aligned} u_* + v_* &= u_\ell + v_\ell, \quad u_* - v_* = u_r - v_r; \\ \left(\frac{\partial u}{\partial t}\right)_* + \left(\frac{\partial v}{\partial t}\right)_* &= -a(u'_\ell + v'_\ell), \quad \left(\frac{\partial u}{\partial t}\right)_* - \left(\frac{\partial v}{\partial t}\right)_* = a(u'_r - v'_r). \end{aligned} \quad (16)$$

Then, in turn, we obtain \mathbf{u}_* and $(\partial \mathbf{u} / \partial t)_*$ by solving the pairs of linear equations (16).

The crucial point in the above process is that the assembled quantity $u + v$ (resp. $u - v$) is continuous across the discontinuity $x + at = 0$ (resp. $x - at = 0$). It has several implications:

- (1) The assembled quantities $u + v$ and $u - v$, corresponding to the Riemann invariants for (1), are used to achieve the claim (12). More precisely, take a look at the characteristic $x = -at$, across which, as mentioned above, both u and v are discontinuous. However, $u + v$ is regular there and the singularity along $x = -at$ has been removed solely onto $u - v$. Then we can manipulate $u + v$ as a scalar variable for a single linear advection equation.
- (2) In smooth regions, the Lax–Wendroff approach can be used to define the instantaneous time derivatives of (proper) assembled variables, which are replaced by the spatial derivatives.
- (3) The resulting pair of linear equations are then solved to obtain the instantaneous time derivatives of primitive variables finally.

It seems that this is the only reasonable way to extend a scalar case to the system (13) in order to construct the numerical flux with the least numerical dissipation under the second order MUSCL-type initial condition. The GRP methodology for (1) uses almost the same idea: look for Riemann invariants, extract singularities, and derive a pair of linear equations (9), particularly in the resolution of rarefaction waves. Since the entropy variable is necessarily taken as one of Riemann invariants and exactly computed, the rarefaction wave can be well resolved so that the resulting scheme is able to capture both (even very strong) rarefaction and shocks waves. Let us illuminate this in some detail. We fix the case of the left-moving rarefaction wave associated with the characteristic field $U - c$, c is the sound speed, as shown in Fig. 2. The primitive variables (ρ, U, p) (or the conservative variables $(\rho, \rho U, \rho E)$) are singular through the rarefaction wave, particularly around the origin. Use the Riemann invariants $\psi(\rho, U, p) = U + \frac{2c}{\gamma-1}$ and S (for polytropic gases, and similarly for general gases) to write (1) in terms of ψ and S as

$$\begin{aligned} \psi_t + (U + c)\psi_x &= TS_x, \\ S_t + US_x &= 0, \end{aligned} \quad (17)$$

where T is the temperature. Since ψ keeps invariant across the centered isentropic rarefaction wave (CRW) in the associated Riemann problem, it behaves exactly like $u + v$ for (13) and be smooth through the entire curved rarefaction wave in the generalized Riemann problem. Therefore, we can use the regularity property of ψ across the rarefaction wave so that usual calculus manipulations can be made. The singularity of the solution is removed onto another variable $\phi = U - \frac{2c}{\gamma-1}$ that satisfies

$$\phi_t + (U - c)\phi_x = TS_x. \quad (18)$$

Note that ϕ is also a Riemann invariant but associated with another characteristic field $U + c$. We resolve (17) to obtain the first equation of (9).

The second equation of (9) can be obtained through tracing the right-going shock trajectory, following van Leer's idea [29].

The source terms in (17) and (18) reflect the variation of entropy as the initial state is not uniform. This variation is well captured in the GRP scheme, and then the variable ψ is resolved subsequently in an analytical way, using the Lax–Wendroff

approach. Due to the regularity of ψ and S and their analytical resolution, it is expected that the rarefaction wave can be captured very accurately using the GRP scheme, and it is indeed. The detail can be found in [6,5].

2.2. The gas-kinetic scheme

In this section, a directional splitting method to solve the 2D BGK equation will be presented. The BGK model in the x -direction can be written as [9]

$$f_t + uf_x = \frac{g - f}{\tau}, \quad (19)$$

where f is the gas distribution function, g is the equilibrium state approached by f , and τ is the particle collision time. Both f and g are functions of space x , time t , particle velocities (u, v) , and internal variable ξ . The particle collision time τ is related to the viscosity and heat conduction coefficients. The equilibrium state is a Maxwellian distribution,

$$g = \rho \left(\frac{\lambda}{\pi} \right)^{\frac{K+2}{2}} e^{-\lambda((u-U)^2 + (v-V)^2 + \xi^2)},$$

where ρ is the density, U and V are the macroscopic velocities in the x and y directions, as in (1), and $\lambda = m/2kT$, where m is the molecular mass, k is the Boltzmann constant, and T is the temperature. Within the equilibrium state g , the ideal gas equation of state is implicitly imposed because the pressure p evaluated from g will be equal to $p = \rho/2\lambda = \rho RT$. For a 2D flow with explicit account of U and V velocities, the random particle motion in the z direction is included into the internal variable ξ , and the total number of degrees of freedom K in ξ is equal to $(5 - 3\gamma)/(\gamma - 1) + 1$. For example, for a diatomic molecular in the 2D simulation, K will be equal to 3, which accounts for the molecule random motion in the z -direction and two rotational degrees of freedom. In the equilibrium state, the internal variable ξ^2 is equal to $\xi^2 = \xi_1^2 + \xi_2^2 + \dots + \xi_K^2$. The relation between mass ρ , momentum ($n = \rho U$, $m = \rho V$), and energy ρE densities with the distribution function f is

$$\begin{pmatrix} \rho \\ n \\ m \\ \rho E \end{pmatrix} = \int \psi_\alpha f d\Xi, \quad \alpha = 1, 2, 3, 4, \quad (20)$$

where ψ_α is the component of the vector of moments

$$\psi = (\psi_1, \psi_2, \psi_3, \psi_4)^\top = \left(1, u, v, \frac{1}{2}(u^2 + v^2 + \xi^2) \right)^\top$$

and $d\Xi = dudvd\xi$ is the volume element in the phase space with $d\xi = d\xi_1 d\xi_2 \dots d\xi_K$. Since mass, momentum and energy are conserved during particle collisions, f and g satisfy the conservation constraint,

$$\int (g - f) \psi_\alpha d\Xi = 0, \quad \alpha = 1, 2, 3, 4, \quad (21)$$

at any point in space and time. For a local equilibrium state with $f = g$, the Euler equations can be obtained by taking the moments of ψ_α to Eq. (19). This yields

$$\int \psi_\alpha (g_t + ug_x) d\Xi = 0, \quad \alpha = 1, 2, 3, 4$$

and the corresponding Euler equations in the x -direction will be the same as Eq. (1). The general solution f of the BGK model (19) at a cell interface $x_{j+1/2}$ and time t is

$$f(x_{j+1/2}, t, u, v, \xi) = \frac{1}{\tau} \int_0^t g(x', t', u, v, \xi) e^{-(t-t')/\tau} dt' + e^{-t/\tau} f_0(x_{j+1/2} - ut), \quad (22)$$

where $x' = x_{j+1/2} - u(t - t')$ is the particle trajectory and f_0 is the initial gas distribution function f at the beginning of each time step ($t = 0$). Two unknowns g and f_0 must be specified in Eq. (22) in order to obtain the solution f . In order to simplify the notation, $x_{j+1/2} = 0$ will be used in the following text. Based on the MUSCL-type reconstruction for the macroscopic variables at a cell interface, the initial gas distribution function f_0 has the corresponding form,

$$f_0 = \begin{cases} g^l [1 + a^l x - \tau(a^l u + A^l)], & x \leq 0, \\ g^r [1 + a^r x - \tau(a^r u + A^r)], & x \geq 0, \end{cases} \quad (23)$$

where the terms being proportional to τ are the nonequilibrium states obtained from the Chapman–Enskog expansion of the BGK model. The parameters of (a^l, A^l, a^r, A^r) are related to the Taylor expansion of a Maxwellian. The nonequilibrium parts have no direct contribution to the conservative variables, i.e.,

$$\begin{aligned} \int (a^l u + A^l) \psi g^l d\Xi &= 0, \\ \int (a^r u + A^r) \psi g^r d\Xi &= 0. \end{aligned} \quad (24)$$

After having f_0 , the equilibrium state g around $(x = 0, t = 0)$ is assumed to have two slopes,

$$g = g_0[1 + (1 - H[x])\bar{a}^l x + H[x]\bar{a}^r x + \bar{A}t], \quad (25)$$

where $H[x]$ is the Heaviside function defined as

$$H[x] = \begin{cases} 0, & x < 0, \\ 1, & x \geq 0. \end{cases}$$

Here g_0 is a local Maxwellian distribution function located at $x = 0$. Even though, g is continuous at $x = 0$, but it has different slopes at $x < 0$ and $x > 0$. In both f_0 and g , a^l, A^l, a^r, A^r , and \bar{A} are related to the derivatives of Maxwellians in space and time. Detailed formulation can be found in [32].

In the reconstruction stage, we have obtained the distributions $\bar{\rho}_j(x), \bar{m}_j(x), \bar{n}_j(x)$, and $\rho_j \bar{E}_j(x)$ inside each cell $x_{j-1/2} \leq x \leq x_{j+1/2}$. At the cell interface $x_{j+1/2}$, the left and right macroscopic states are

$$\mathbf{u}_j(x_{j+1/2}) = \begin{pmatrix} \bar{\rho}_j(x_{j+1/2}) \\ \bar{m}_j(x_{j+1/2}) \\ \bar{n}_j(x_{j+1/2}) \\ \bar{\rho} \bar{E}_j(x_{j+1/2}) \end{pmatrix}, \quad \mathbf{u}_{j+1}(x_{j+1/2}) = \begin{pmatrix} \bar{\rho}_{j+1}(x_{j+1/2}) \\ \bar{m}_{j+1}(x_{j+1/2}) \\ \bar{n}_{j+1}(x_{j+1/2}) \\ \bar{\rho} \bar{E}_{j+1}(x_{j+1/2}) \end{pmatrix}.$$

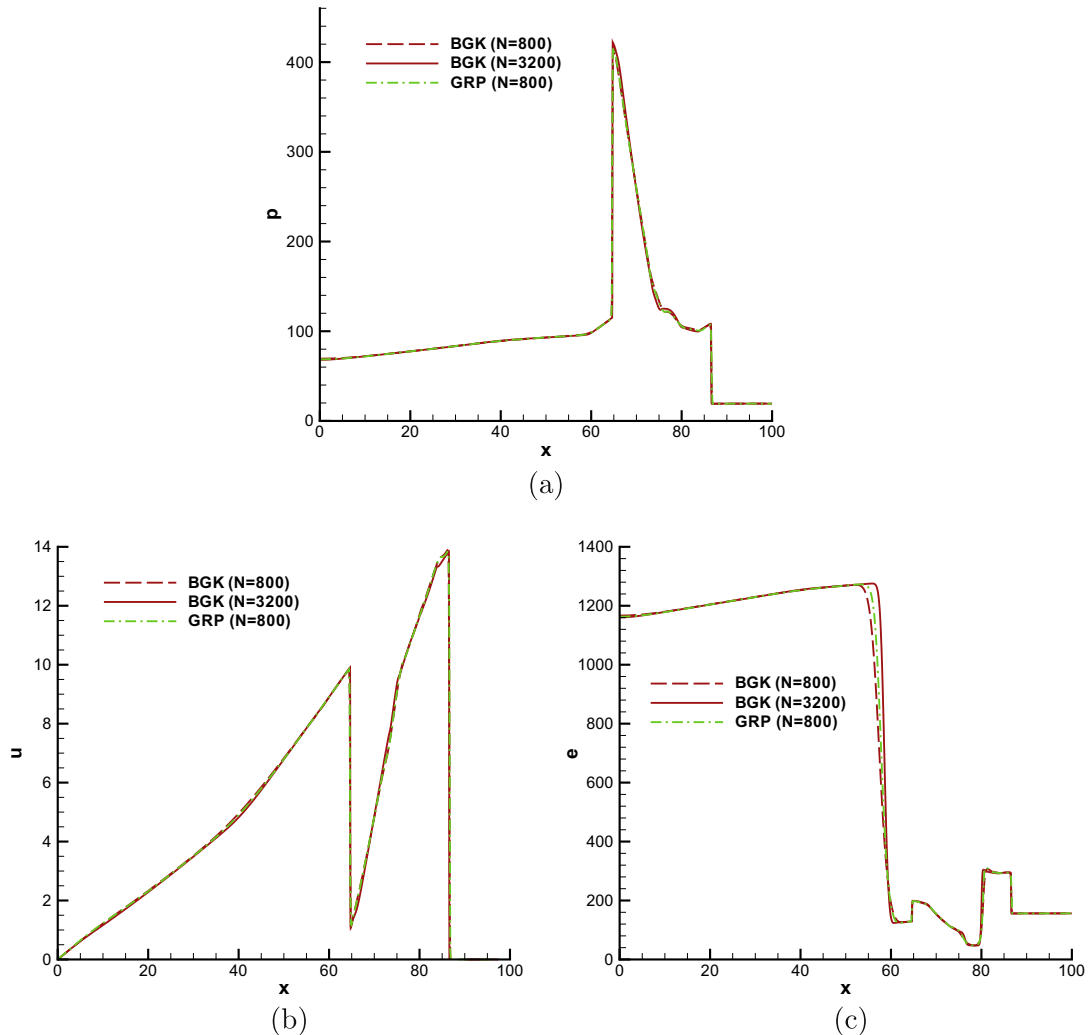


Fig. 3. Woodward-Colella blast wave problem. (a) pressure, (b) velocity, (c) internal energy.

By using the relation between the gas distribution function f and the macroscopic variables (Eq. (20)), at $x_{j+1/2}$ we get

$$\int g^l \psi d\Xi = \mathbf{u}_j(x_{j+1/2}); \int g^l a^l \psi d\Xi = \frac{\mathbf{u}_j(x_{j+1/2}) - \mathbf{u}_j(x_j)}{\Delta x^-}, \quad (26)$$

$$\int g^r \psi d\Xi = \mathbf{u}_{j+1}(x_{j+1/2}); \int g^r a^r \psi d\Xi = \frac{\mathbf{u}_{j+1}(x_{j+1}) - \mathbf{u}_{j+1}(x_{j+1/2})}{\Delta x^+}, \quad (27)$$

where $\Delta x^- = x_{j+1/2} - x_j$ and $\Delta x^+ = x_{j+1} - x_{j+1/2}$. Based on the above equations, all parameters in the initial distribution function f_0 can be fully determined.

After determining f_0 , the corresponding values of ρ_0, U_0, V_0 and λ_0 in g_0 of Eq. (25), i.e.,

$$g_0 = \rho_0 \left(\frac{\lambda_0}{\pi} \right)^{\frac{K+2}{2}} e^{-\lambda_0((u-U_0)^2 + (v-V_0)^2 + \zeta^2)},$$

can be determined as follows. Taking the limit $t \rightarrow 0$ in Eq. (22) and substituting its solution into Eq. (21), the conservation constraint at $(x = x_{j+1/2}, t = 0)$ gives

$$\int g_0 \psi d\Xi = \mathbf{u}_0 = \int_{u>0} \int g^l \psi d\Xi + \int_{u<0} \int g^r \psi d\Xi, \quad (28)$$

where $\mathbf{u}_0 = (\rho_0, m_0, n_0, \rho_0 E_0)^T$ are the macroscopic conservative flow variables located at the cell interface at time $t = 0$.

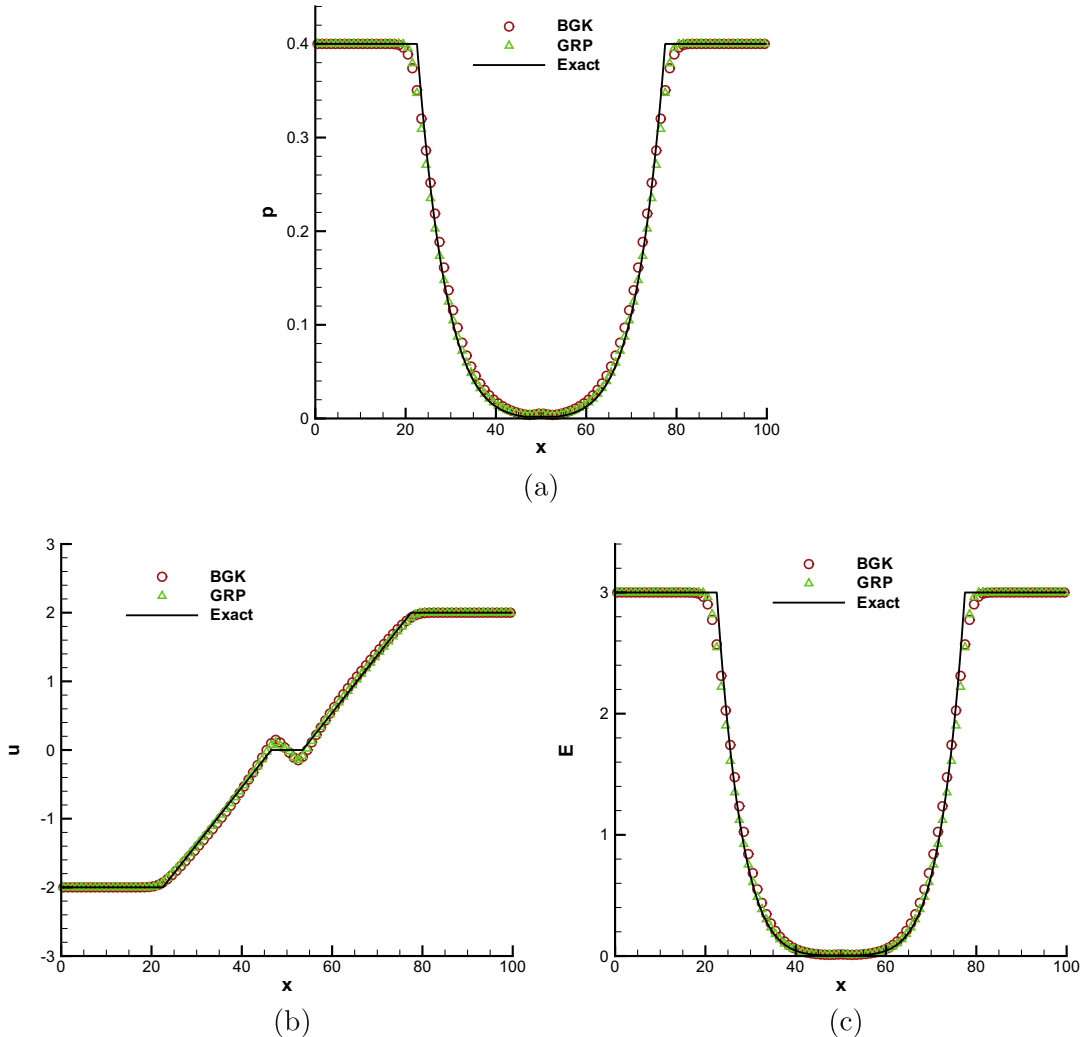


Fig. 4. Sjolgreen's low density problem. (a) pressure, (b) velocity, (c) energy.

Then, \bar{a}^l and \bar{a}^r of g in Eq. (25) can be obtained through the relation of

$$\frac{\mathbf{u}_{j+1}(x_{j+1}) - \mathbf{u}_0}{\rho_0 \Delta x^+} = \bar{M}_{\alpha\beta}^0 \begin{pmatrix} \bar{a}_1^r \\ \bar{a}_2^r \\ \bar{a}_3^r \\ \bar{a}_4^r \end{pmatrix} = \bar{M}_{\alpha\beta}^0 \bar{a}_\beta^r \quad (29)$$

and

$$\frac{\mathbf{u}_0 - \mathbf{u}_j(x_j)}{\rho_0 \Delta x^-} = \bar{M}_{\alpha\beta}^0 \begin{pmatrix} \bar{a}_1^l \\ \bar{a}_2^l \\ \bar{a}_3^l \\ \bar{a}_4^l \end{pmatrix} = \bar{M}_{\alpha\beta}^0 \bar{a}_\beta^l, \quad (30)$$

where the matrix $\bar{M}_{\alpha\beta}^0 = \int g_0 \psi_\alpha \psi_\beta d\Xi / \rho_0$ is known.

Up to this point, we have determined all parameters in the initial gas distribution function f_0 and the equilibrium state g at the beginning of each time step $t = 0$. After substituting Eqs. (23) and (25) into Eq. (22), the gas distribution function f at a cell interface can be expressed as

$$\begin{aligned} f(x_{j+1/2}, t, u, v, \xi) = & (1 - e^{-t/\tau})g_0 + (\tau(-1 + e^{-t/\tau}) + te^{-t/\tau})(\bar{a}^l H[u] + \bar{a}^r (1 - H[u]))ug_0 + \tau(t/\tau - 1 + e^{-t/\tau})\bar{A}g_0 \\ & + e^{-t/\tau}((1 - u(t + \tau)\bar{a}^l)H[u]g^l + (1 - u(t + \tau)\bar{a}^r)(1 - H[u])g^r) \\ & + e^{-t/\tau}(-\tau\bar{A}^l H[u]g^l - \tau\bar{A}^r (1 - H[u])g^r). \end{aligned} \quad (31)$$

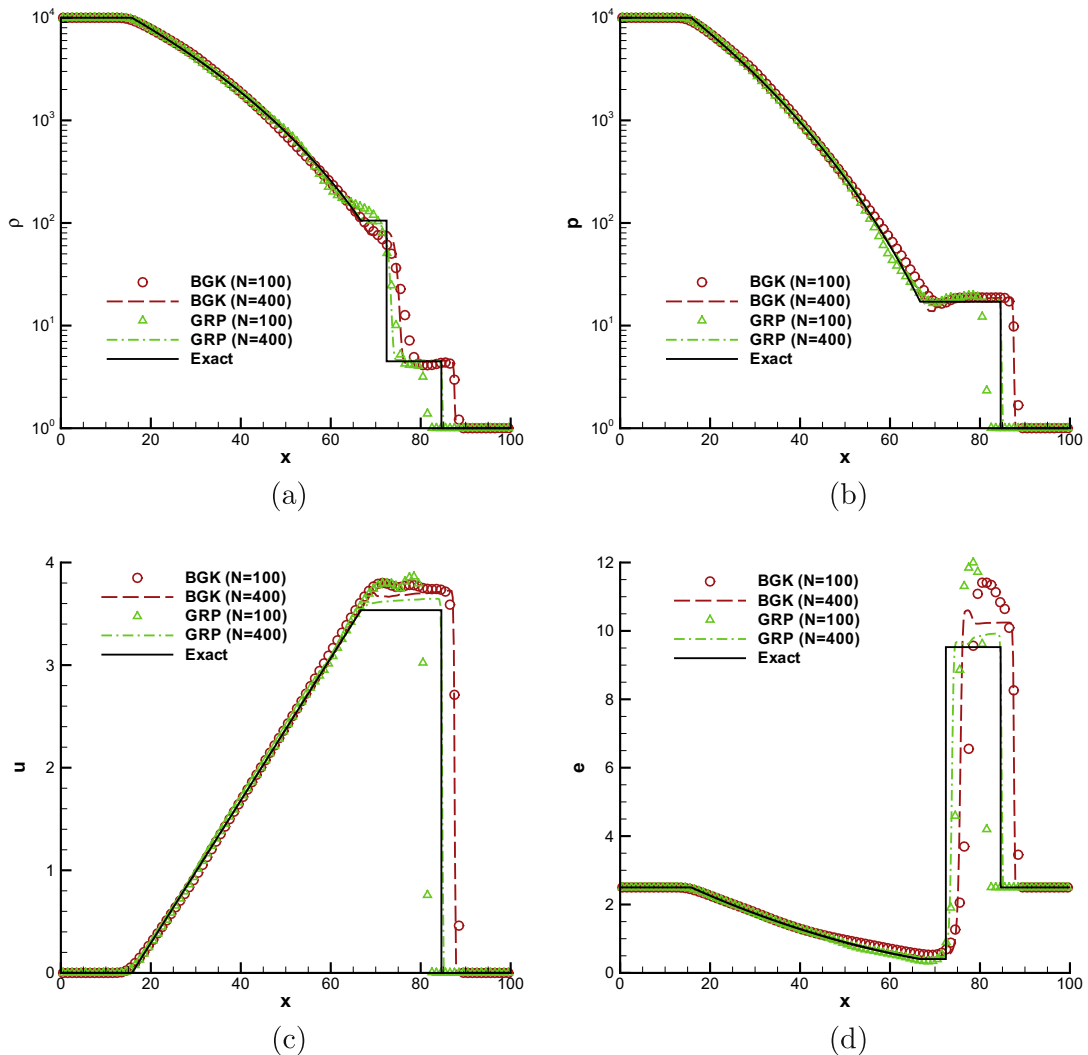


Fig. 5. Large density ratio problem. (a) density, (b) pressure, (c) velocity, (d) internal energy.

The only unknown left in the above expression is \bar{A} . Since both f (Eq. (31)) and g (Eq. (25)) contain \bar{A} , the integration of the conservation constraint Eq. (21) at $x_{j+1/2}$ over the whole time step Δt gives

$$\int_0^{\Delta t} \int (g - f) \psi dtd\Xi = 0.$$

The evaluation of \bar{A} is about to get time variation of macroscopic variables at a cell interface, which is similar to the GRP in the evaluations of $(\partial U / \partial t)_*$ and $(\partial p / \partial t)_*$.

Finally, the time-dependent numerical fluxes in the x -direction across the cell interface can be computed as

$$\begin{pmatrix} F_\rho \\ F_m \\ F_n \\ F_{pE} \end{pmatrix}_{j+1/2} = \int \begin{pmatrix} 1 \\ u \\ v \\ \frac{1}{2}(u^2 + v^2 + \xi^2) \end{pmatrix} f(x_{j+1/2}, t, u, v, \xi) d\Xi, \quad (32)$$

where $f(x_{j+1/2}, t, u, v, \xi)$ is given in Eq. (31). By integrating the above equation to the whole time step, we can get the total mass, momentum and energy transport. For the Euler solutions, theoretically the particle collision time τ should approach to zero in order to keep the equilibrium state everywhere. As a result, the only terms left in (31) will be these related to the equilibrium one, which has the similar mechanism as the Riemann solver. However, the molecules in any flow system have limited mean free path and particle collision time. Starting from a discontinuity, the flow behavior will depend on the ratio between the time passed and particle collision time. The formulation (31) describes such a relaxation process from the mol-

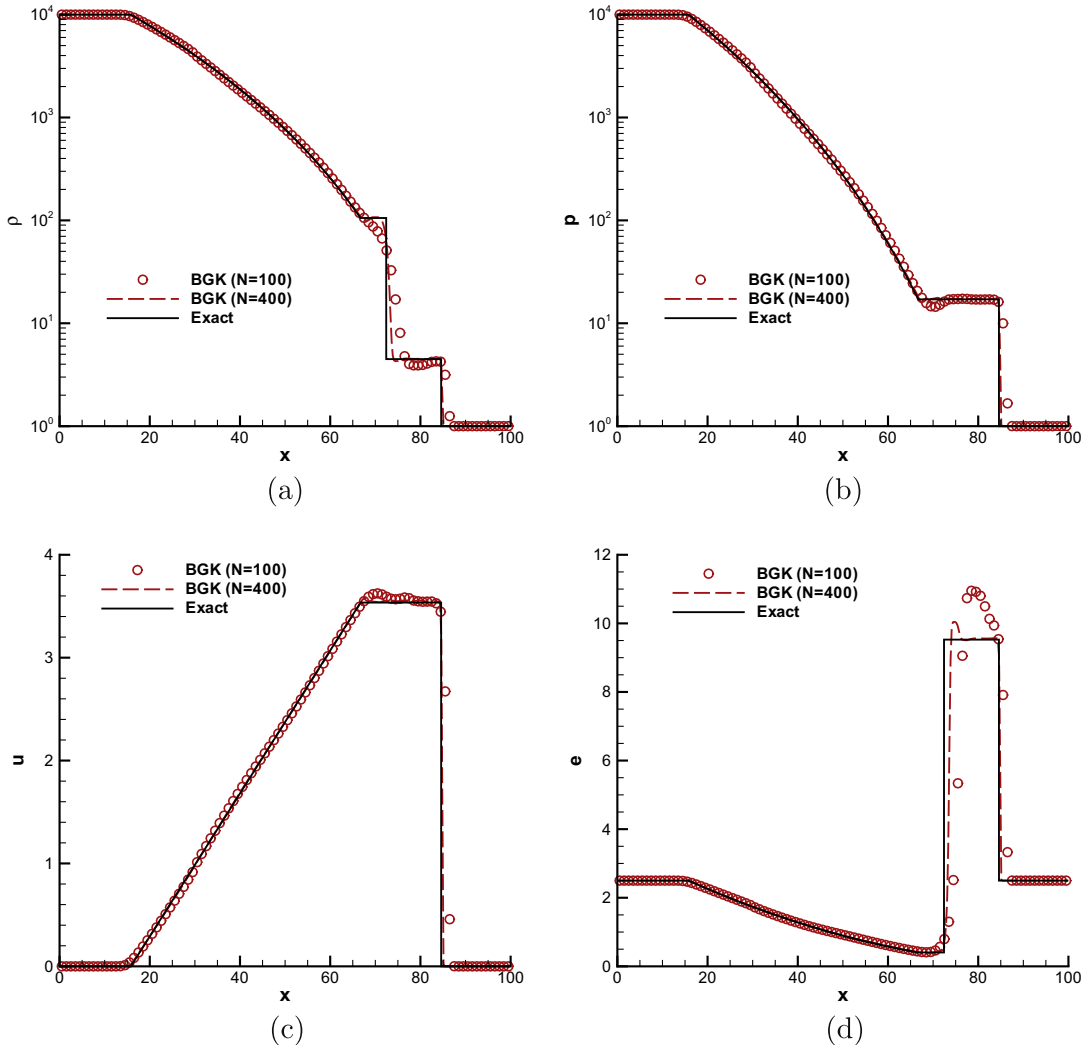


Fig. 6. Large density ratio problem. (a) density, (b) pressure, (c) velocity, (d) internal energy.

ecule free transport to the equilibrium state formation. The Euler solution is achieved only in the limiting case of $t/\tau \rightarrow \infty$. Theoretically, the particle collision time τ is equal to the mean free path over particle speed. In a discretized space, due to the limited cell resolution we will not have infinite flow structure resolution. Therefore, the particle mean free path needs to take account of the cell resolution as well. For the Euler solution, which has no any characteristic scale, the mean free path can be assumed to be proportional to the cell size. The collision time used in all test cases in this paper have the following form,

$$\tau = \Delta x \sqrt{\lambda_0} (\alpha + \beta |p^l - p^r| / (p^l + p^r)) \quad (33)$$

with $\alpha = 0.05$ and $\beta = 1.0$, where λ_0 is given in the equilibrium state g_0 , and p^l and p^r are the pressure jump at the cell interface in the initial reconstructed data. The consideration for the above formulation is the following. As mesh size goes to zero, τ will go to zero as well, and the GKS converges to the Euler solutions. In comparison with flux vector splitting scheme, with the above definition of particle collision time there will have tens of particle collisions within each time step. In other words, the numerical dissipation introduced in the above formulation is much less than that in the flux vector splitting method.

In the continuum flow regime, the initial free transport part in the gas distribution function (31) disappears. The evolution of continuous flow will converge to the equilibrium state quickly. However, in the dissipative shock region, the numerical particle mean free path is much enlarged to capture the non-equilibrium effect, such as the real physical process inside a shock layer. This is equivalent to enlarging the physical shock thickness to the cell size scale, and the GKS provides the particle transport and collision mechanism here.

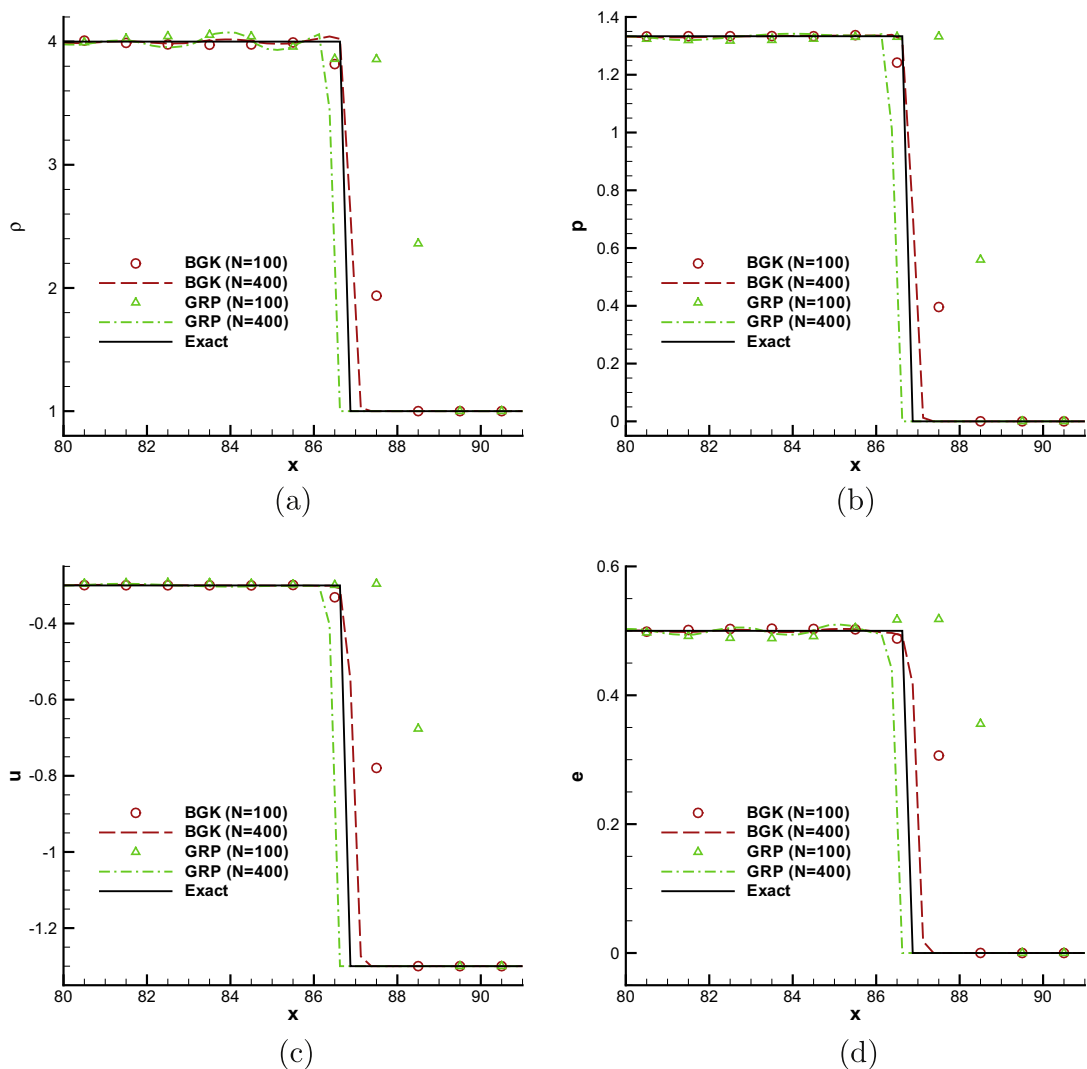


Fig. 7. Slowly moving shock problem. (a) density, (b) pressure, (c) velocity, (d) internal energy.

3. Details of the test cases

In this section we will present quite full comparison of numerical results by the GRP and GKS schemes. These examples are all very challenging, ranging from several one-dimensional blast wave problem to the high speed flow impinging on a cylinder. Unless otherwise stated, the van Leer limiter is adopted and the CFL number is set to be 0.5. Since GRP and GKS use the identical van Leer limiter for the conservative flow variables reconstruction, any difference in the simulation results is due to the flux function, i.e., the mechanism of gas evolution models around a cell interface. Since GRP is truthfully solving the Euler equations and the GKS is following the kinetic equation, the comparison distinguishes the effects of different physical processes on the simulation results.

3.1. Problems in one-dimensional space

3.1.1. Woodward–Colella blast wave problem

We first show the interacting blast wave problem proposed in [30]. The diatomic gas is initially at rest, and the density is everywhere unit. The pressure is $p = 1000$ for $0 \leq x < 10$ and $p = 100$ for $90 < x \leq 100$, while it is only $p = 0.01$ in $10 < x < 90$. Reflecting boundary conditions are applied at both ends. Numerical results with 800 grid points are shown in Fig. 3 to exhibit the performance of both schemes. This test case clearly demonstrates the capability of both schemes in the capturing of strong shock waves. The GRP presents a little bit sharper solution than the GKS in the internal energy distribution.

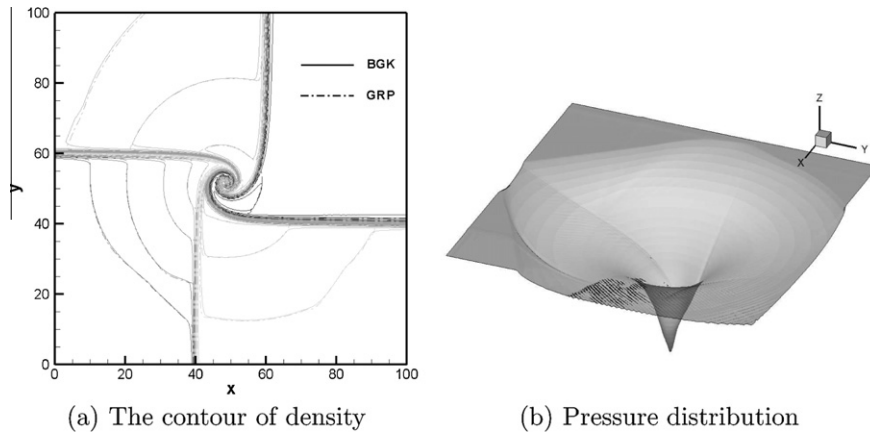


Fig. 8. Formation of spiral in the 2D Riemann problem.

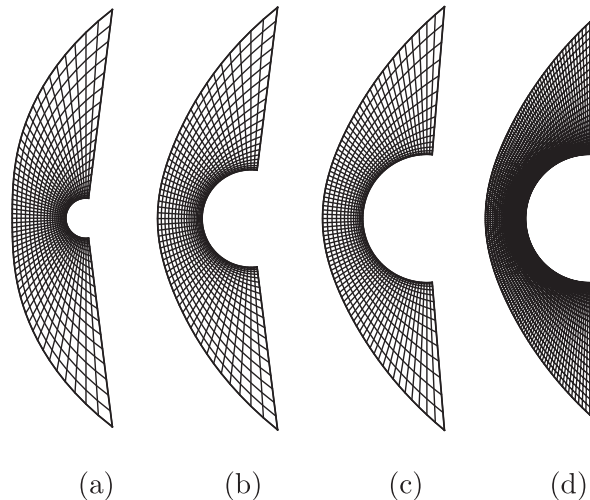


Fig. 9. Meshes in cylinder case. (a) 54×20 , (b) 54×20 , (c) 80×14 , (d) 160×28 .

3.1.2. Low density problem

This example was first proposed in [10] for demonstrating the ability of a numerical scheme to preserve the positivity of density and internal energy. In contrast to the blast wave problem, this test shows strong rarefaction waves. The initial data is given with $(\rho, U, p) = (1, -2, 0.4)$ for $0 \leq x < 50$ and $(\rho, U, p) = (1, 2, 0.4)$ for $50 \leq x \leq 100$. The number of grid points used here is 100. Both schemes work well, as shown in Fig. 4. Many approximate Riemann solvers may fail in this test case [10].

3.2. Large density ratio problem

This example was proposed in [27] to test the ability to capture extremely strong rarefaction wave and its influence on the shock location. In the original paper, it shows that most MUSCL-type schemes have defects in resolving, even with very fine mesh, the correct wave structures. In this problem, initially the pressure and density ratio between two neighboring states are very high. The initial data is $(\rho, U, p) = (10000, 0, 10000)$ for $0 \leq x < 30$ and $(\rho, U, p) = (1, 0, 1)$ for

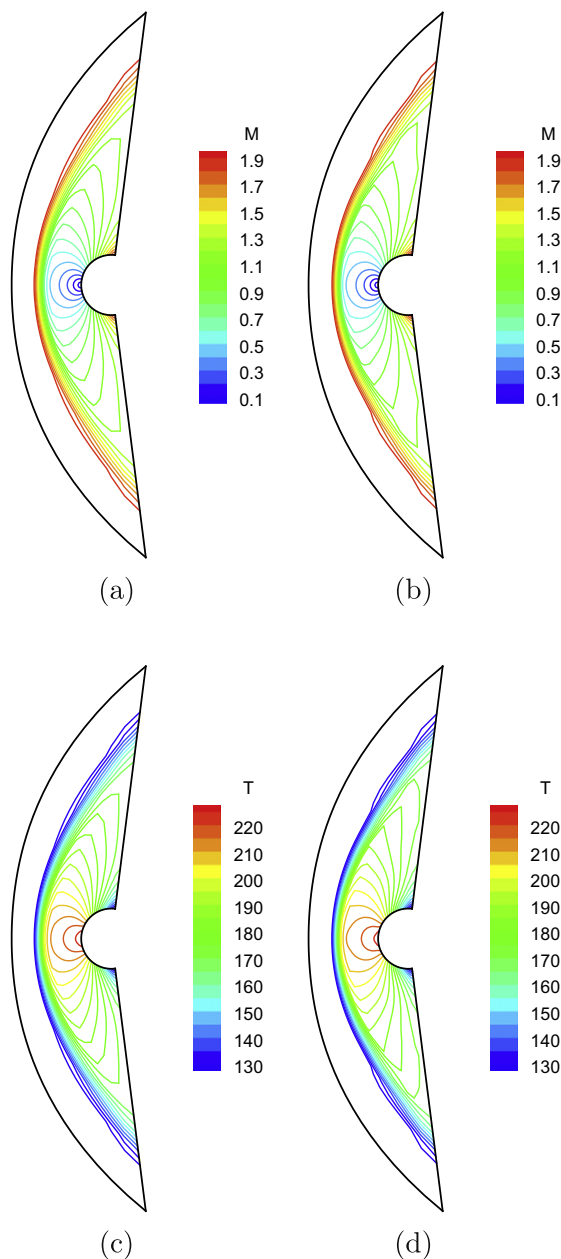


Fig. 10. $M = 2$ Case with mesh (a). The left column is computed by the GKS and the right by the GRP.

$30 \leq x \leq 100$. CFL number is set as 0.32. The results with 100 and 400 points from both GRP and GKS are shown in Fig. 5. For GRP, from 100 to 400 grid points, the shock location converges to the correct position. With 400 grid points, the GRP scheme gives perfect results, which can be comparable to those from very high resolution schemes, i.e., the fifth order WENO scheme with 10000 grid points [27]. Surprisingly, the GKS presents the same shock front location with 100 and 400 grid points. One of the reason is that the GKS solves viscous governing equations, but the exact solution is the inviscid one. In order to clarify the situation, we reduce the particle collision time in Eq. (33) to $\alpha = \beta = 10^{-4}$. With the reducing of dissipation, the GKS results with 100 and 400 grid points are shown in Fig. 6. Again, the GKS keeps almost the same shock location for 100 and 400 grid points. Even with 100 grid points, it can capture the solution very well. This clearly demonstrates that the GKS converges to the inviscid Euler solution as the particle collision time reduces. In the coarse mesh cases, this test clearly shows that the shock speed of GRP is slower than that of GKS. This is probably due to the starting error in the first few time steps from the initial strong discontinuity. The detail reason needs further investigation.

3.3. Slowly moving shock

This is a test case for strong slowly moving shock with the minmod limiter for both schemes. The initial data is: $(\rho, U, p) = (4.0, 0.3, 4/3)$ for $0 \leq x < 20$; and $(\rho, U, p) = (1.0, -1.3, 10^{-6})$ for $20 < x \leq 100$. The polytropic index is taken to be $\gamma = 5/3$. This is an almost infinite strong shock in the sense that the density ratio is close to its maximum.

The simulation results from both 100 and 400 grid points are shown in Fig. 7. The shock fronts are captured crisply by both schemes. In the coarse mesh with 100 grid points, the GKS has a better shock location. As the mesh is refined, both schemes converge to the exact solution. The GKS generates less magnitude of post-shock oscillation than GRP.

The above several examples are fully recognized as severe test problems and many shock capturing schemes may fail to provide accurate or even correct results, such as the correct position of shock front in [27]. The GRP and GKS encounter no difficulties for these cases. One of the reason is that both schemes can compute the entropy accurately. As a result, the rarefaction wave is resolved perfectly, so is the shock location. Also, through the comparison we can realize that the accuracy of GKS in obtaining the inviscid Euler solutions even though it targets on the kinetic model.

3.4. Problems in two-dimensions

In comparison with the 1D test cases, two-dimensional simulations are much more interesting and challenging. The GRP is basically 1D gas evolution model. In order to make GKS be consistent with GRP, we adapt the direction splitting GKS here in all simulations. A multi-dimensional GKS scheme has been developed as well [33]. In the 2D case, some classical test problems such as double Mach reflection have been reported in [15,32] using these two schemes. Here we choose two problems of interaction of (compressible) vortex sheets and the flow impinging on a cylinder. The CFL number is set to be 0.5 and 0.7, respectively.

3.4.1. Formation of spiral through the interaction of vortex sheets

This is a special case of 2D Riemann problems formulated in [34] to simulate the formation of spirals, see also [19,15] for the solution structure. The initial data is a constant state in each quadrant: $(\rho, U, V, p) = (0.5, 0.5, -0.5, 5)$ for $x > 0, y > 0$, $(\rho, U, V, p) = (1.0, 0.5, 0.5, 5)$ for $x < 0, y > 0$, $(\rho, U, V, p) = (2.0, -0.5, 0.5, 5)$ for $x < 0, y < 0$, $(\rho, U, V, p) = (1.5,$

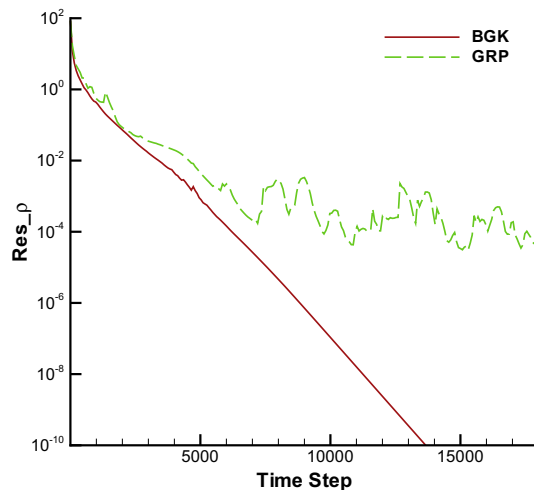


Fig. 11. $M = 2$ Case with mesh (a). Convergence residue distribution.

$-0.5, -0.5, 5)$ for $x > 0, y < 0$. Initially four vortex sheets are supported, respectively, on the x - and y -axes with the same sign, but they have different amounts of measures. They interact immediately after $t > 0$ to generate a spiral in the center and the state there closes to the vacuum. We can see the wonderful performance of both schemes from Fig. 8 by the comparison with those in [26,22,17].

3.4.2. Flow impinging on a cylinder

For the blunt body simulations, we test flows with Mach number 2, 5 and 10. Also, four meshes have been used, which are shown in Fig. 9. We call them mesh (a), (b), (c) and (d). The difference between mesh (a) and (b) comes from the different size of the computational domains to account for the standoff distance of the bow shock. The length–width (circumferential–radial) ratio of Mesh (c) is a little smaller. Mesh (d) is a refined version of mesh (c) with double grid points in both directions. At $M = 2$ with mesh (a), GRP and GKS can capture the flow structure nicely in front of the cylinder, which are shown in Fig. 10 for the Mach number and temperature distributions. The residual for both calculation is shown in Fig. 11. The GKS

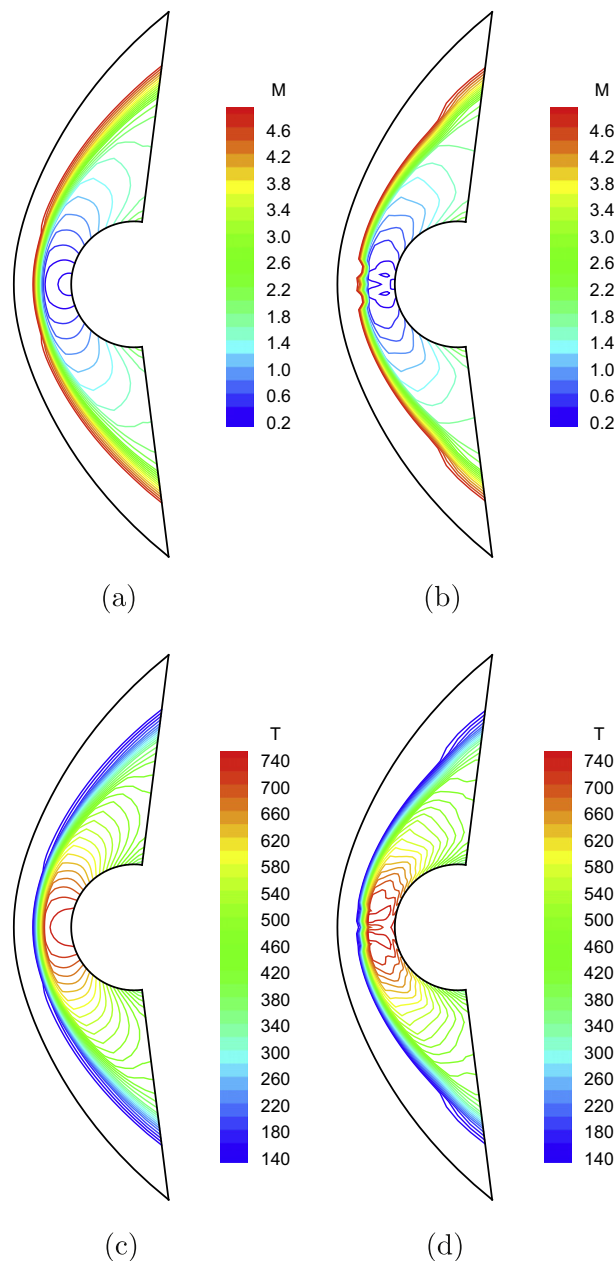


Fig. 12. $M = 5$ Case with mesh (b). The left column is computed by the GKS and the right by the GRP.

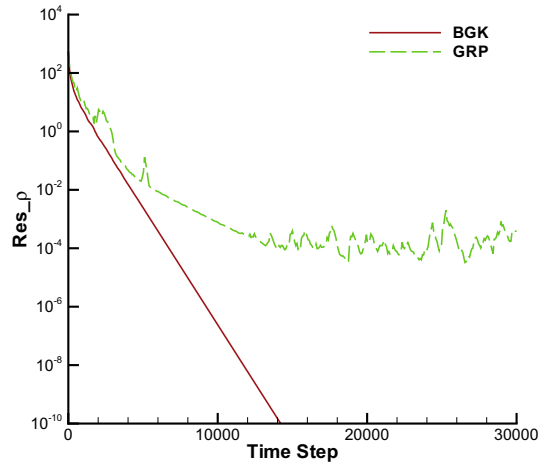


Fig. 13. $M = 5$ Case with mesh (b). Convergence residue distribution.

converges to machine zero quickly and the convergence of GRP is saturated at 10^{-4} . At $M = 5$ with mesh (b), the simulation results from GRP and GKS are shown in Fig. 12 as well as the convergence rate in Fig. 13. At $M = 5$, even with convergent results, GRP has difficulty in capturing a smooth solution in front of the cylinder. It seems that GRP converges to another solution. This may raise the question about the uniqueness of the Euler solution. For GKS, the same as $M = 2$ case, it presents a nice result. As we increase the Mach number to 10, with the same mesh (b), the GKS and GRP results are shown in Fig. 14. Surprisingly, GRP presents a smooth solution in comparison with $M = 5$ case, even though it still has wiggles around sonic lines. However, for the $M = 10$ case, with mesh (c) the simulation results from GKS and GRP are shown in Fig. 15. To further validate mesh convergence, the computation is also done with mesh (d), as shown in Fig. 16. Again, GRP presents oscillatory results and the calculations break down eventually. Even with the first order Godunov method, an oscillatory solutions will be obtained as well. In both $M = 10$ calculation with different meshes, GKS converges to machine zero in the same way as $M = 5$ case.

In the cylinder case, both GKS and GRP are using the identical mesh and reconstruction scheme. Any difference is coming from the flux evaluation. Since GRP is so truthfully solving the Euler equations under the corresponding initial condition, the simulation results clearly demonstrate the fundamental flaws in solving the inviscid Euler equations for the capturing of hypersonic flow in the blunt body calculation. Even with the fatal results from GRP, theoretically we do not know how to fix it, since the GRP is so accurately solving the Euler equations. In the cylinder case, the flow structure is relatively simple. The flaws in the GRP must come from its representation of the numerical shock layer in multi-dimensional case. As we know, with limited cell resolution, a physical shock structure is enlarged up to the mesh size scale. Inside the shock layer, a highly non-equilibrium state is present. This non-equilibrium state can be captured by following real physical process of particle transport and collision. This is somehow consistent the mechanism underlying the GKS, where the free transport and collision are both included in the flux evaluation. However, from the starting point, GRP assumes an equilibrium state everywhere, even inside the numerical shock layer. GRP lacks the mechanism to construct a non-equilibrium shock layer on the mesh size scale, and it has inappropriate physical mechanism in its flux construction there. Therefore, it is fundamentally flawed to use the Euler equations as a foundation in the construction of shock capturing scheme. More analysis will be presented in the next section.

In terms of computational efficiency, the flux calculation of GRP spends only a little bit more time, say 5%, than the first-order exact Riemann solver (Godunov). At Mach number 2, the times of GRP and GKS spending on flux calculation including reconstruction are nearly the same, which is about 1:1.04 between GRP and GKS for $M = 2$ case. Here the computational time is the averaged one over the whole flow field, since the cost of GRP solver is different in different flow region due to its different number of inner iteration. Furthermore, with the current computational power, the time spending on the flux evaluation in a code takes only a small fraction of total computational time in a software. With the same order of computational cost, the accuracy of the modeling seems more important than using inaccurate cheaper flux replacements.

4. Discussion

In terms of Riemann solver, the GRP provides the most accurate flux function for the Euler equations under piecewise linearly discontinuous initial distribution. The wave interaction and modification of the characteristics due to spatial variation of initial flow variables have been fully included in GRP. The scheme used in this paper is probably the ultimate one people can construct under the piecewise discontinuous initial condition. Different from many other approximate Riemann solvers, the GRP is truthfully solving the Euler equations. This is also the reason why the current comparison is important.

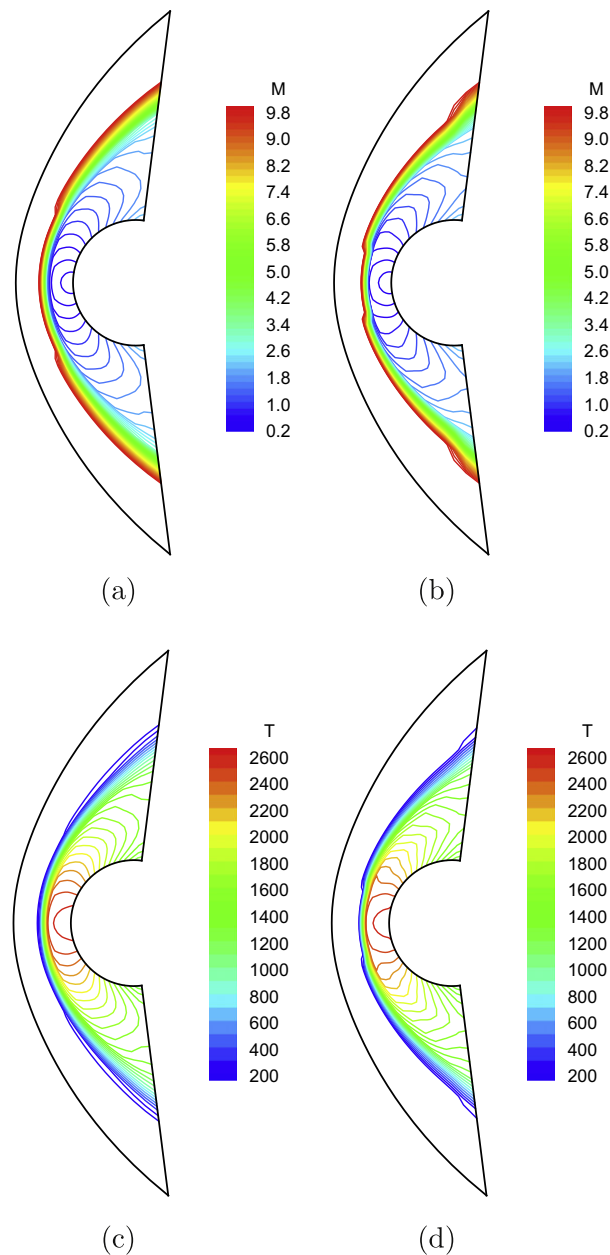


Fig. 14. $M = 10$ Case with mesh (b). The left column is computed by the GKS and the right by the GRP.

Through the numerical tests, we may answer the question about the validity of using and solving the Euler equations in a discretized space, even for the inviscid flow. Even though the GKS solves the Boltzmann equation, it presents accurate Euler solutions as well. In all tests, GRP and GKS are using the identical initial reconstruction, any difference in the simulation results is coming from the mechanism of constructing the flux function. Even with different underlying governing equations, the GRP and GKS have close similarity in the construction of local solution. Both schemes present a time-dependent flow evolution from an initially discontinuous data. In smooth flow regions, both methods go back to the traditional Lax–Wendroff method, where the spatial derivatives are used to get the temporal variation.

The GRP and GKS present different mechanism to describe the flow evolution from a discontinuity. For the GRP, in order to get all kinds of distinct waves in the generalized Riemann solution, it assumes that there is intensive particle collision and the gas sets down to the equilibrium state instantaneously everywhere, even inside a highly dissipative shock layer. This assumption may not be valid in a highly dissipative flow region. The GKS first presents particle free transport process from an initially discontinuous data, then through the particle collision it generates the dissipative wave structure. With intensive

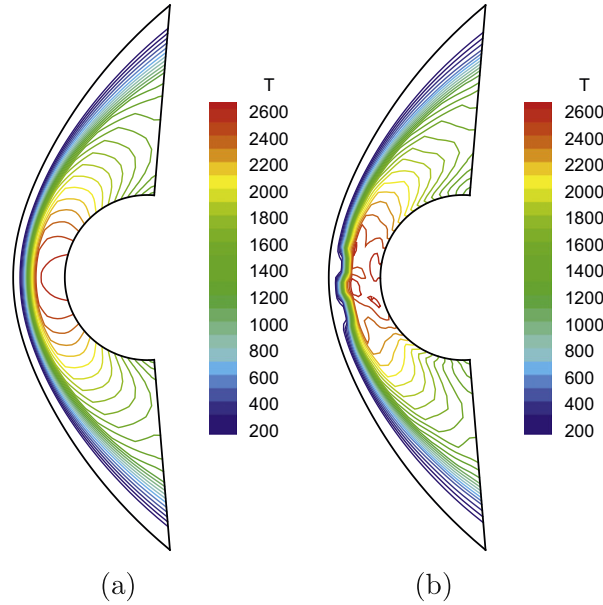


Fig. 15. $M = 10$ Case with mesh (c). The left is temperature distribution computed by the GKS and the right by the GRP.

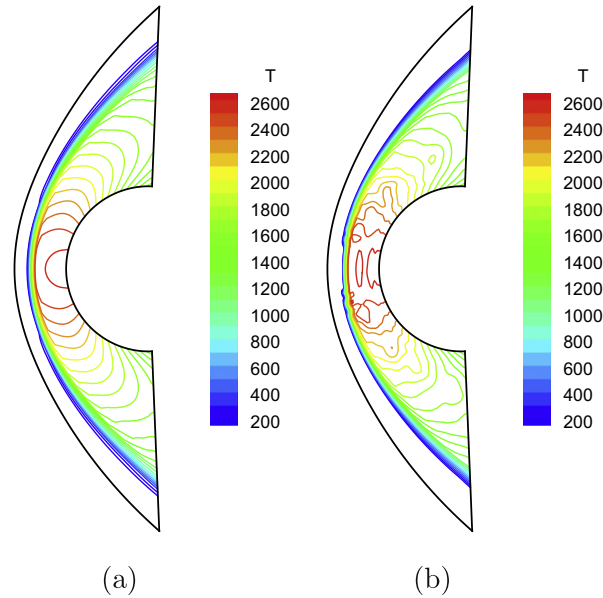


Fig. 16. $M = 10$ Case with mesh (d). The left is temperature distribution computed by the GKS and the right by the GRP.

particle collisions within a time step, a Navier–Stokes gas distribution function can be obtained from the GKS. The Euler solution is considered only as a limiting case when $t/\tau \rightarrow \infty$. The physical mechanism of the GKS can be hardly described using any macroscopic governing equation. Theoretically, the BGK equation itself provides a mechanism for the transport and collision on a scale of $\Delta x \rightarrow 0$ and $\Delta t \rightarrow 0$. Through the inclusion of initial discontinuity in a scale of $\Delta x \neq 0$ and $\Delta t \neq 0$, the local gas evolution in the GKS takes account of cell resolution effect, and its solution may not be fully consistent with the BGK equation. More importantly, the GKS uses the transport and collision mechanism of the BGK equation in its modeling and construction of numerical algorithm.

A numerical shock layer needs to be considered as an enlarged physical shock structure. Since the shock thickness is on the order of particle mean free path, an enlarged numerical shock layer, i.e., across a few mesh size, requires a numerical cell size to be comparable with the pseudo-particle mean free path. Therefore, on the scale of mesh size, the non-equilibrium

flow physics has to be taken into account in the gas evolution process in the discontinuous region. As we know, as a particle moves across a shock layer, there is only limited number of particles collisions. The non-equilibrium shock structure is constructed through the competition between particle free transport and collisions. This non-equilibrium process provides the appropriate dissipation for the smooth transition from one equilibrium upstream state to another equilibrium downstream state. For the same numerical shock layer, the GRP replaces the non-equilibrium physical reality by an equilibrium one with the assumption of infinite number of particle collisions. The equilibrium state used inside a shock layer cannot provide enough numerical dissipation, especially in multi-dimensional case. Therefore, the use of the Euler equations in the flux modeling is not valid in the non-equilibrium region. The GKS follows closely the flow physics. The initial free transport, which provides the dissipation, depends closely on the jump of the discontinuity. This amount of dissipation can be hardly pre-assigned in a governing equation because the jump itself has numerical uncertainties, such as the use of different limiters. The trigger of shock instability for GRP in high Mach number cases is due to the absence of non-equilibrium mechanism to provide “adjustable” dissipation in its flux function. Certainly, there exists various on-going studies in carbuncle problem [24,11,16,25,31], and the problem is not yet resolved. The paper provides an alternative explanation for this problem. The value of the current analysis is that it is based on the mechanism beyond the Euler equations itself. Actually, this analysis is consistent with the reason given in [24], which states “the carbuncle phenomenon is connected to those solutions of the Riemann Problem that explicitly take into account the contact surface; this fact is usually shown by its occurrence in flux difference splitting approaches; the explicit treatment of the contact surface seems to be the essential point of the problem”. As we know, for the exact Euler solution, there are infinite number of particle collisions which prevent the penetration of particles crossing each other at the contact surface, the so-called keeping the sharp contact surface. For GKS, the particle penetration due to the relaxation process exist all the time and cannot be fully removed.

Through this study, we may think of the possible direction for the further development of CFD algorithms. Since GRP is truthfully solving the Euler equations under the generalized initial condition, the absence of non-equilibrium mechanism in the Euler solutions shows that the Euler equations cannot be properly used as governing equations for numerical fluid in a discretized space. Due to the limited cell resolution, any zero thickness discontinuity in the Euler solution will be enlarged numerically. As a consequence, the corresponding flow physics inside this dissipative layer has to be accounted for by the numerical scheme. One may think of using the Navier–Stokes equations with dissipative terms to capture the corresponding physical process inside the non-equilibrium layer. But, this cannot be valid as well, because the NS equations have only the physical dissipation on the hydrodynamic scale, which cannot be properly used to describe the flow behavior in the kinetic scale, such the flow evolution starting from an initial discontinuity. In other words, the dissipation provided in the governing equations should be able to adjust itself according to the locally reconstructed data.

Due to the cell resolution, to introduce a numerical discontinuity in a shock capturing scheme is necessary. The main idea we would like to deliver through this research is that for a shock capturing scheme we need a correct physical mechanism to model the gas evolution from such a discontinuity in the discretized space. The Euler equations cannot provide such a correct physical mechanism. The real physics from a discontinuity is that the particles take free transport first, then particle collisions drive the system towards to equilibrium state. The GKS constructs such a physical process from a discontinuity with the help of the gas-kinetic BGK equation.

5. Conclusion

In this paper, we have made a detailed comparison between two well-developed numerical methods for compressible flow computations, i.e., the generalized Riemann solver and the gas-kinetic scheme, by simulating many 1D and 2D test cases. The comparison is made in terms of the accuracy, efficiency, and robustness of each method. The present study indicates that the GRP and GKS can both be applied to inviscid compressible flow computations in 1D case, and can give comparable predictions. GRP is slightly more computational efficient than GKS, but GKS is more robust than GRP. For the 2D blunt body simulations, the performance of GRP and GKS deviates. Like many other Riemann solvers, the GRP has intrinsic shock instability in the high Mach number flow computations. Since the initial reconstruction used in both GRP and GKS are identical, any difference is coming from the flux evaluation mechanism. Through the comparison of evolution mechanism in GRP and GKS, it is realized that, even for the inviscid flow in a space with limited resolution, the Euler equations cannot provide a valid physical mechanism in the numerical strong shock layer. When modeling high Mach number flows, it is necessary to introduce discontinuities and to enlarge the non-equilibrium layer to the cell size scale in the discretized space. To take account of the physics in such a scale, the direct modeling of the particle evolution process is preferred, rather than direct adaptation of well-defined macroscopic governing equations which are valid in continuous space and time.

Acknowledgements

This paper is done when the first two authors visit Hong Kong University of Science and Technology, whose hospitality and support are greatly appreciated. J. Li is partially supported by the Key Program from Beijing Educational Commission (KZ200910028002), PHR (IHLB) and NSFC (10971142, 11031001). Q. B. Li is supported by National Natural Science Foundation of China (Project No. 10872112 and 10932005). K. Xu is supported by Hong Kong Research Grant Council 621709 and

RPC10SC11, National Natural Science Foundation of China (Project No. 10928205), National Key Basic Research Program (2009CB724101).

References

- [1] M. Ben-Artzi, The generalized Riemann problem for reactive flows, *J. Comput. Phys.* 81 (1989) 70–101.
- [2] M. Ben-Artzi, J. Falcovitz, A second-order Godunov-type scheme for compressible fluid dynamics, *J. Comput. Phys.* 55 (1984) 1–32.
- [3] M. Ben-Artzi, J. Falcovitz, An upwind second-order scheme for compressible duct flows, *SIAM J. Sci. Stat. Comput.* 7 (1986) 744–768.
- [4] M. Ben-Artzi, J. Falcovitz, *Generalized Riemann Problems in Computational Fluid Dynamics*, Cambridge University Press, 2003.
- [5] M. Ben-Artzi, J. Li, Hyperbolic balance laws: Riemann invariants and the generalized Riemann problem, *Numer. Math.* 106 (2007) 369–425.
- [6] M. Ben-Artzi, J. Li, G. Warnecke, A direct Eulerian GRP scheme for compressible fluid flows, *J. Comput. Phys.* 218 (2006) 19–34.
- [7] P.L. Bhatnagar, E.P. Gross, M. Krook, A model for collision processes in gases I: small amplitude processes in charged and neutral one-component systems, *Phys. Rev.* 94 (1954) 511–525.
- [8] J.P. Boris, D.L. Book, Flux-corrected transport. I. SHASTA, a fluid transport algorithm that works, *J. Comput. Phys.* 11 (1973) 38–69.
- [9] S. Chapman, T.G. Cowling, *The Mathematical Theory of Non-Uniform Gases*, third ed., Cambridge University Press, Cambridge, 1970.
- [10] B. Einfeldt, C.D. Munz, P.L. Roe, B. Sjögren, On Godunov-type methods near low densities, *J. Comput. Phys.* 92 (1991) 273–295.
- [11] V. Elling, The carbuncle phenomenon is incurable, *Acta Math. Sci.* 29 (2009) 1647–1656.
- [12] J. Falcovitz, G. Alfandary, G. Hanoch, A 2-D conservation laws scheme for compressible flows with moving boundaries, *J. Comput. Phys.* 138 (1997) 83–102.
- [13] J. Falcovitz, A. Birman, A singularities tracking conservation laws scheme for compressible duct flows, *J. Comput. Phys.* 115 (1994) 431–439.
- [14] S.K. Godunov, A finite difference method for the numerical computation and discontinuous solutions of the equations of fluid dynamics, *Mat. Sb.* 47 (1959) 271–295.
- [15] E. Han, J. Li, H.Z. Tang, Accuracy of the adaptive GRP scheme and the simulation of 2-D Riemann problems for compressible Euler equations, *Commun. Comput. Phys.*, in press.
- [16] K. Kitamura, P. Roe, F. Ismail, Evaluation of Euler fluxes for hypersonic flow computations, *AIAA J.* 47 (2009) 44–53.
- [17] A. Kurganov, E. Tadmor, Solution of two-dimensional Riemann problems for gas dynamics without Riemann problem solvers, *Numer. Methods Part. Diff. Eqs.* 18 (2002) 584–608.
- [18] J. Li, G. Chen, The generalized Riemann problem method for the shallow water equations with bottom topography, *Int. J. Numer. Methods Eng.* 65 (2006) 834–862.
- [19] J. Li, T. Zhang, S. Yang, *The Two-Dimensional Riemann Problem in Gas Dynamics*, Addison Wesley Longman, 1998.
- [20] Q.B. Li, S. Fu, K. Xu, A compressible Navier–Stokes flow solver with scalar transport, *J. Comput. Phys.* 204 (2005) 692–714.
- [21] Q.B. Li, S. Fu, K. Xu, Application of BGK scheme with kinetic boundary conditions in hypersonic flow, *AIAA J.* 43 (2005) 2170–2176.
- [22] X.D. Liu, P.D. Lax, Solution of two-dimensional Riemann problems of gas dynamics by positive schemes, *SIAM J. Sci. Comput.* 19 (1998) 319–340.
- [23] T. Ohwada, On the construction of kinetic schemes, *J. Comput. Phys.* 166 (2001) 271–301.
- [24] M. Pandolfi, D. D'Ambrosio, Numerical instabilities in upwind methods: analysis and cures for the Carbuncle phenomenon, *J. Comput. Phys.* 177 (2002) 156–175.
- [25] X.Y. Ren, A robust shock-capturing scheme based on rotated Riemann solvers, *Comput. Fluids* 32 (2003) 1379–1403.
- [26] C.W. Schulz-Rinne, J.P. Collins, H.M. Glaz, Numerical solution of the Riemann problem for two-dimensional gas dynamics, *SIAM J. Sci. Comput.* 14 (1993) 1394–1414.
- [27] H.Z. Tang, T.G. Liu, A note on the conservative schemes for the Euler equations, *J. Comput. Phys.* 218 (2006) 451–459.
- [28] E.F. Toro, *Riemann Solvers and Numerical Methods for Fluid Dynamics: A Practical Introduction*, Springer, 1997.
- [29] B. van Leer, Towards the ultimate conservative difference scheme V, *J. Comput. Phys.* 32 (1979) 101–136.
- [30] P. Woodward, P. Colella, The numerical simulation of two-dimensional fluid flow with strong shocks, *J. Comput. Phys.* 54 (1984) 115–173.
- [31] H. Wu, L. Shen, Z. Shen, Numerical method to cure numerical shock instability, *Commun. Comput. Phys.* 8 (2010) 1264–1271.
- [32] K. Xu, A gas-kinetic BGK scheme for the Navier–Stokes equations and its connection with artificial dissipation and Godunov method, *J. Comput. Phys.* 171 (2001) 289–335.
- [33] K. Xu, M.L. Mao, L. Tang, A multidimensional gas-kinetic BGK scheme for hypersonic viscous flow, *J. Comput. Phys.* 203 (2005) 405–421.
- [34] T. Zhang, Y. Zheng, Conjecture on the structure of solutions of the Riemann problem for two-dimensional gas dynamics systems, *SIAM J. Math. Anal.* 21 (1990) 593–630.